Supplement of: Enhancement of ammonium nitrate aerosol in the Northern Hemisphere lower stratosphere linked to Asian summer monsoon outflow

F. Ekinci[1,2*,5], O. Eppers[2*], O. Appel[1,2*], F. Ploeger[3,10], A. Dragoneas[8], S. Molleker[7], P. Brauner[2*], H.-C. Lachnitt[1], F. Weyland[1], L. Ort[9], N. Emig[1], H.-C. Clemen[2*], L. Tomsche[1,4], M. Ebert[5], P. Hoor[1], B. Vogel[3], Y. Cheng[6], J. Schneider[2*], S. Borrmann[1,2], and F. Köllner[1,2*]

[1]Institute for Atmospheric Physics, University of Mainz, Mainz, Germany
[2]Particle Chemistry Department, Max Planck Institute for Chemistry, Mainz, Germany
[3]Institute of Climate and Energy Systems (ICE-4), Forschungszentrum Jülich, Jülich, Germany
[4]Institut für Physik der Atmosphäre, Deutsches Zentrum für Luft- und Raumfahrt (DLR), Oberpfaffenhofen, Germany
[5]Institute for Applied Geosciences (Environmental Mineralogy), Technical University of Darmstadt, Darmstadt, Germany
[6]Aerosol Chemistry Department, Max Planck Institute for Chemistry, Mainz, Germany
[7]Instrument Development Group, Max Planck Institute for Chemistry, Mainz, Germany
[8]Climate Geochemistry Department, Max Planck Institute for Chemistry, Mainz, Germany
[9]Atmospheric Chemistry Department, Max Planck Institute for Chemistry, Mainz, Germany
[10]Institute for Atmospheric and Environmental Research, University of Wuppertal, Wuppertal, Germany
[*]now at: Aerosol Chemistry Department, Max Planck Institute for Chemistry, Mainz, Germany

Correspondence: F. Köllner (f.koellner@mpic.de)

S1. HALO Aerosol Submicrometer Inlet (HASI)

S1.1 Description of HASI System

The HASI (HALO Aerosol Submicrometer Inlet) is designed to sample submicrometer aerosol particles for in-situ measurements onboard the research aircraft. It provides a controlled airflow of up to 30 liters per minute, distributed among four sampling lines that supply aerosol measurement instruments inside the aircraft with sampling air. The inlet is mounted on top of the aircraft fuselage to ensure representative sampling of ambient aerosols, avoiding disturbances from the aircraft boundary layer. The HASI system decelerates incoming airflow by a factor of ~40 through a three-stage process comprising a front shroud, a main diffuser, and smaller diffusers at the tips of the sampling tubes. An optional backward-facing sampling tube is also available for alternative measurement configurations. The design minimizes the entry of large cloud droplets and ice crystals, reducing potential measurement artifacts (Minikin et al., 2017; Andreae et al., 2018). During the PHILEAS campaign in 2023, the HASI system was used for the ERICA and the FASD (Fast Aerosol Size Distribution; Leibniz Institute for Tropospheric Research (TROPOS)) instrument for submicron aerosol sampling. To maintain accurate aerosol sampling, the HASI system is operated under isokinetic conditions, where the airflow velocity at the inlet matches the aircraft's airspeed. The so-called HASI Flow Control Unit (HASI-FCU) regulates the sample flow rate during flights, using pumps and bypass lines to

ensure consistency. During PHILEAS, in certain instances, the HASI-FCU malfunctioned, failing to provide sufficient bypass flow for isokinetic sampling. This issue was attributed either to software problems and/or the failure of the by pass pumps. In Table S1 all measurement events that were affected by this are listed and analyzed in Sect. S1.2.

Table S1: HASI-FCU Shutdown events: All listed measurement events correspond to when the bypass flow responsible for isokinetic sampling dropped.

Flight	**HASI-FCU operation problems (start time – end time)**
F01	2023-07-25 10:27:47 – 13:22:14
F02	2023-08-06 06:25:18 – 06:48:07; 2023-08-06 07:11:47 – 08:17:59
F04	2023-08-10 07:39:50 – 07:42:24; 2023-08-10 07:52:53 – 07:57:43; 2023-08-10 08:20:23 – 08:32:36; 2023-08-10 13:42:34 – 14:16:36; 2023-08-10 14:21:24 – 14:31:34
F05	2023-08-12 06:23:11 – 07:19:18; 2023-08-12 07:20:40 – 07:25:02
F07	2023-08-21 10:05:36 – 10:09:25; 2023-08-21 18:53:36 – 19:24:35
F09	2023-08-28 22:16:10 – 22:36:53; 2023-08-28 23:04:49 – 23:09:34; 2023-08-29 01:00:13 – 01:09:39; 2023-08-29 02:59:46 – 03:18:01
F14	2023-09-10 20:59:28 – 21:21:35; 2023-09-10 21:44:57 – 21:56:19
F15	2023-09-14 01:18:37 – 02:15:33
F16	2023-09-15 22:05:21 – 22:10:23
F17	2023-09-16 21:56:13 – 22:54:10; 2023-09-17 05:43:44 – 06:27:59
F18	2023-09-19 18:00:01 – 18:34:18; 2023-09-20 01:15:49 – 01:32:56; 2023-09-20 01:36:39 – 02:16:09
F19	2023-09-22 21:39:58 – 21:48:51; 2023-09-22 21:50:32 – 21:54:21; 2023-09-22 21:59:16 – 22:03:49; 2023-09-22 22:13:21 – 22:15:53; 2023-09-22 23:19:42 – 23:39:46; 2023-09-23 00:00:55 – 00:12:16; 2023-09-23 00:34:32 – 00:52:24; 2023-09-23 01:40:08 – 01:56:13; 2023-09-23 02:16:30 – 02:21:49; 2023-09-23 02:32:14 – 02:40:54; 2023-09-23 04:49:11 – 04:52:05; 2023-09-23 05:43:33 – 06:08:00
F20	2023-09-27 07:22:55 – 07:40:25; 2023-09-27 07:41:53 – 07:49:15; 2023-09-27 07:51:35 – 07:56:45; 2023-09-27 08:05:09 – 08:18:43; 2023-09-27 09:18:32 – 09:20:48; 2023-09-27 10:57:17 – 11:01:22

S1.2 Analysis of Isokinetic Flow Regulation and Impact on Measurements

To assess the impact of the HASI-FCU issues on the aerosol mass concentration measurements with ERICA, Flight F18 was analyzed as a representative case. This flight was chosen because the HASI-FCU outage occurred at particularly high altitudes in the UTLS region, the primary region of interest for this study. The measurement conditions during F18 are thus well-suited for evaluating potential sampling artifacts under the most relevant atmospheric conditions.

A malfunction of the HASI-FCU interrupts the bypass flow necessary for maintaining isokinetic sampling at the aircraft inlet. Sampling theory distinguishes between isokinetic, sub-isokinetic, and super-isokinetic conditions, depending on the relationship between the sampling flow (V_0) and the velocity of the surrounding airstream (V_1). Under isokinetic conditions ($V_1 = V_0$), the sampled particle population is representative of the ambient aerosol. In sub-isokinetic conditions ($V_0 > V_1$), as expected when the bypass pumps are off due to HASI-FCU issue, larger particles are preferentially enriched in the inlet system. This is because large particles, owing to their momentum, cannot easily follow the streamlines and are more likely to enter the inlet, potentially resulting in artificially increased mass concentrations. In contrast, under super-isokinetic conditions ($V_0 < V_1$), small particles are preferentially sampled (Kulkarni et al., 2011).

Despite these theoretical considerations, analysis of the ERICA-AMS and ERICA-SkyOPC (model Sky-OPC, Series 1.129, GRIMM Aerosol Technik Ainring GmbH & Co. KG) data for Flight F18 (Fig. S1) reveals no evidence of sudden or artificial increases in aerosol mass and/or particle number concentrations during periods of the HASI-FCU issue. Both the ERICA-AMS and the -SkyOPC show consistent values throughout the HASI-FCU outage, indicating that the HASI-FCU issue did not impact the measurements. This result is likely attributable to the aerosol size distribution in the UTLS, which is dominated by particles smaller than $1\,\mu\mathrm{m}$. At high altitudes, larger particles are generally absent, and thus the bias expected from sub-isokinetic sampling does not materialize. All HASI-FCU failure events across the UTLS dataset were systematically examined, and no significant artifacts or changes in AMS and/or SkyOPC concentrations were observed during any of these events. These findings underscore the robustness of AMS and SkyOPC measurements in the UTLS, even in the presence of temporary inlet control failures.

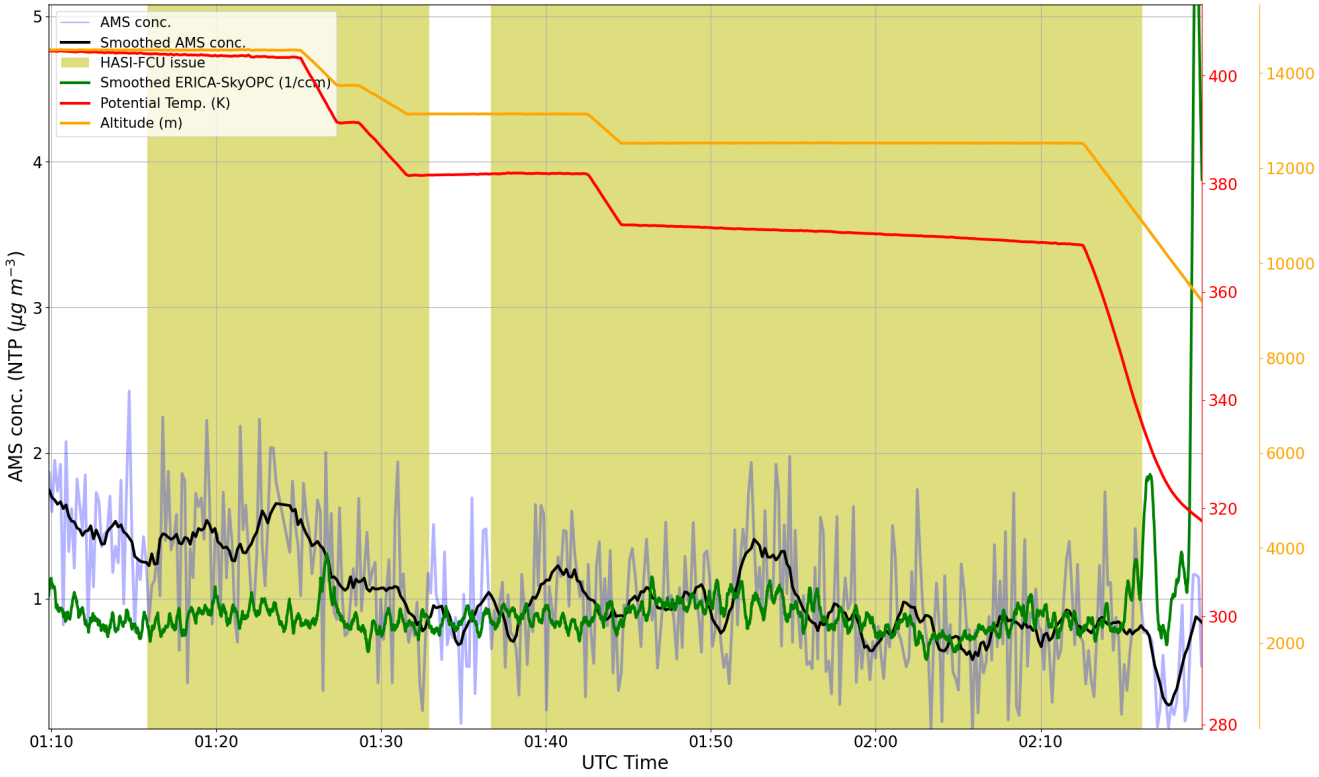

Figure S1. Time series of AMS total aerosol mass concentration (gray, smoothed in black; in $\mu g\ m^{-3}$) and smoothed ERICA-SkyOPC particle number concentration (green; in ccm^{-1}) during HASI-FCU issues for Flight F18. Yellow-shaded regions mark periods of HASI-FCU malfunction. Altitude (orange; in m) and potential temperature (red; in K) are shown for reference. Despite HASI-FCU control outages at high altitudes, neither AMS nor SkyOPC data exhibit sudden increases or artifacts, indicating no measurable impact on aerosol measurements. These findings are consistent with all other HASI-FCU events in the UTLS analyzed in this study.

S2. ERICA-LAMS: Data Evaluation

S2.1 Data Post-Processing

In the following, we will present the post-processing steps necessary to analysis ERICA-LAMS single particle spectra. First, a zero-offset correction was applied to eliminate baseline signals, followed by a threshold of 1 mV for both cations and anions to differentiate real particle from noise spectra (see Tab. S2 'Noisy-Spectra'). This was done immediately after the flights in order to remove the empty spectra that contained only noise. Second, the HASI inlet used for particle sampling during flights was not suitable for measurements inside clouds. Therefore, particle spectra obtained inside clouds were excluded from the further analysis by using a cloud flag derived from the BCPD instrument (Backscatter Cloud Probe with Polarization Detection; Lucke et al. (2023)) (see Tab. S2 'Cloud-Spectra') . The cloud flag was provided by Johannes Lucke (DLR). After these steps, the

remaining particle spectra (referred to as 'Flight-Spectra', Tab. S2) were mass calibrated using the software package CRISP (Klimach, 2012). As a last step, particle spectra with maximum an bipolar ion peak intensity lower than a 5 mV*sample (determined in Sect. S2.2) were not further analyzed. Thus, the number of spectra analyzed in this study is given in Tab. S2 with 'Valid Spectra'. Finally, all particles that occur in the ExLS background air mass after filtering with N2O (< 336 ppbv) and CO (< 40 ppbv) are listed in the column 'ExLS background Spectra'.

Table S2. Overview of number of ERICA-LAMS spectra for all PHILEAS flights used in this study (F04, F06, F07 and F18-F20). The number of usable spectra for each flight is called Flight-Spectra. It represents the number of spectra before the classification for each (event as described in Sect. S4). It includes usable spectra with information about particles without bipolar noise or cloud interactions. Noisy-Spectra are spectra filtered by a threshold of 1 mV for cation and anion signals. Cloud-Spectra are spectra taken during cloud sampling during the flight.

Flight	ExLS background Spectra	Valid Spectra	Flight-Spectra	Noisy-Spectra	Cloud-Spectra
F04	3149	22666	24381	41	4693
F06	3423	18568	19901	44	1617
F07	3837	33128	33818	316	1130
F18	6295	26769	28427	251	1493
F19	11687	30988	32595	44	171
F20	9010	25800	27090	6	579

S2.2 Ion Peak Area Threshold

The ion peak area threshold was introduced by Köllner et al. (2017) in order to distinguish ions signals from background noise. The following criteria were used to determine this threshold: First, all single particle mass spectra sampled during the PHILEAS mission were taken into account. Second, it is assumed that certain m/z values are not occupied by ions from ambient particles by the laser ablation and ionization process. Specifically, m/z +2 to +6 for the positive polarity and m/z -2 to -11 for the negative polarity were considered here. Finally, the threshold was determined at the intersection of the normalized cumulative abundance curve crossing the 99% of the cumulative value, as shown in Fig. S2. Although the results indicated slightly different thresholds for cations (under 5 mV*samples) and anions (under 4 mV*samples), the proximity of these values led to the adoption of a unified threshold of 5 mV*samples for both polarities.

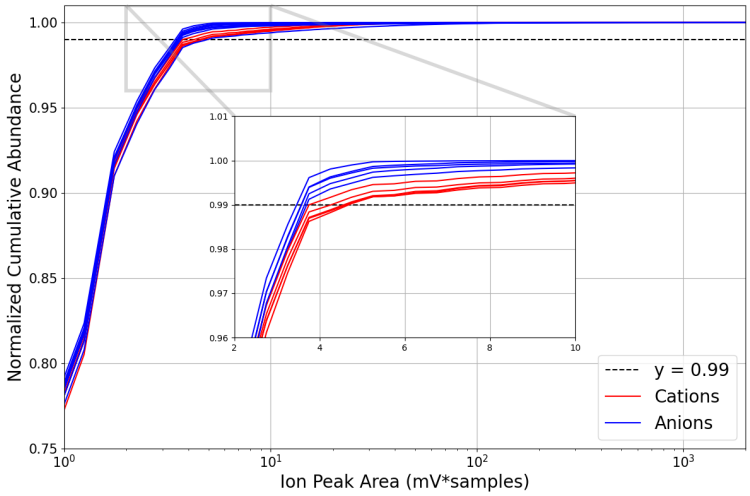

Figure S2. Normalized cumulative abundance of ion signal intensities for of the positive (red) and negative (blue) ion peak areas at m/z +2 to +6 and m/z -2 to -11 (assumed non-occupied m/z values based on Köllner et al. (2017)). The black dashed line indicates the horizontal line for 99%. The inset highlights the region where 99% of the cumulative ion abundance is reached, corresponding to an intensity threshold of approximately 4 mV*samples. To ensure a conservative filtering of noise and retain chemically meaningful signals, we adopted a stricter threshold of 5 mV*samples as the lower limit for ion inclusion in the analysis.

S2.3 Particle Classification: NO^+ – rich and potassium-dominated

The classification method described by Appel et al. (2022a) was used to identify NO^+-rich particles, and the approach outlined by Köllner et al. (2017) was applied to classify potassium-dominated particles. In total, 37,401 particle spectra from flights F04, F06, F07, F18, F19, and F20 were analyzed, restricted to number of particles within ExLS background air masses (as defined in Sect. S4) and with diameters between 200 and 500 nm (defined in Sect. S2.4)

For NO^+-rich particles, spectra with the dominant ion peak at m/z +30 (NO^+) were identified, yielding a total of 12,108 particles of this type. As a subsequent step, the ion marker method was employed to further classify the NO^+-rich particles, determining whether they contain primary compounds such as silicates and potassium (see Tab. S3). The presence of primary marker species in the NO^+-rich particle spectra was assessed by evaluating whether at least one of the following ion signals exceeded a peak area threshold of 5 mV*samples: Si, P, Na, Mg, V, Fe, K, Cr, Zn, Ti, Cu, Li, or Pb. Spectra that met this criterion were classified as 'primary' NO^+-rich particles (1,624 spectra), while those without any of these marker ions above the threshold were categorized as 'secondary' NO^+-rich particles (10,484 spectra). This study focuses on 'secondary' NO^+-rich particle types to be consistent with the analysis in Appel et al. (2022b). The analysis for this study was carried out using this particle type, as according to Appel et al. (2022a), they correspond to particles formed in the ATAL without inclusion of 'primary' compounds. Figures S3a and b show the typical mean spectra of NO^+-rich particles for different air mass periods. Figure S3a is a comparison of the Late Phase and the AMA filaments into the ExLS. Figure S3b is a comparison of the NO^+-

rich particle spectra between the AMA filaments into the ExLS and the lower ATAL regime measured during StratoClim (< 370 K potential temperature). The NO^+-rich particles represent a particle type whose properties correspond well with the signature of the particles measured within the ATAL described by Appel et al. (2022a). Therefore, this particle type is treated as being related to the sources and formation processes of the ATAL throughout this work. However, it is not possible to completely exclude other sources, as we are currently unaware of any other sources for this specific particle type.

For other particle types such as potassium-dominated, the remaining spectra were analyzed using a fuzzy c-means clustering method in CRISP with specific parameters:

- *Ion type*: **Cation**;
- *Preprocessing*: **power each m/z by 0.5**;
- *Normalization*: **Sum**;
- *Distance metric*: **Correlation**;
- *Initialization Startcluster Number/Difference*: **10/0.9**;
- *Fuzzifier/Fuzzy abort*: **1.3/1e^{-5}**.

This clustering yielded four particle types: meteoric material containing particles (7,642 spectra) dominated by m/z +24/+25/+26 (Mg^+) and +54/+56 (Fe^+); potassium-dominated particles (5,151 spectra) with dominant signals at m/z +39/+41 (K^+) (Fig. S3 c); mixed-type particles (4,838 spectra) containing organics, sulfur oxides, and other components; and undefined particles (7,662 spectra) that could not be assigned to the other types.

Table S3. Particle classification by marker species and associated ion markers applied in this study (ion peak area threshold > 5 mV*samples (see Sect. S2.2)).

Ion markers	**Marker species (Threshold > 5 mV)**
m/z -76 (SiO_3^-); m/z -60 (SiO_2^-); m/z +28 (Si^+)	Si (Silicon)
m/z -79 (PO_3^-); m/z -63 (PO_2^-)	P (Phosphorus)
m/z +23 (Na^+)	Na (Sodium)
m/z +24/+25/+26 (Mg^+)	Mg (Magnesium)
m/z +51 (V^+); m/z +67 (VO^+)	V (Vanadium)
m/z +54/+56 (Fe^+)	Fe (Iron)
m/z +39/+41 (K^+)	K (Potassium)
m/z +40 (Ca^+)	Ca (Calcium)
m/z +52/+53 (Cr^+); m/z +68 (CrO^+); m/z +84 (CrO_2^+)	Cr (Chromium)
m/z +64 (TiO^+); m/z +48 (Ti^+)	Ti (Titanium)
m/z +63/+65 (Cu^+)	Cu (Copper)
m/z +7 (Li^+)	Li (Lithium)
m/z +208; m/z +207; m/z +206 (Pb^+)	Pb (Lead)
m/z +202; m/z +199; m/z +200 (Hg^+)	Hg (Mercury)
m/z +64; m/z +66; m/z +68 (Zn^+)	Zn (Zinc)

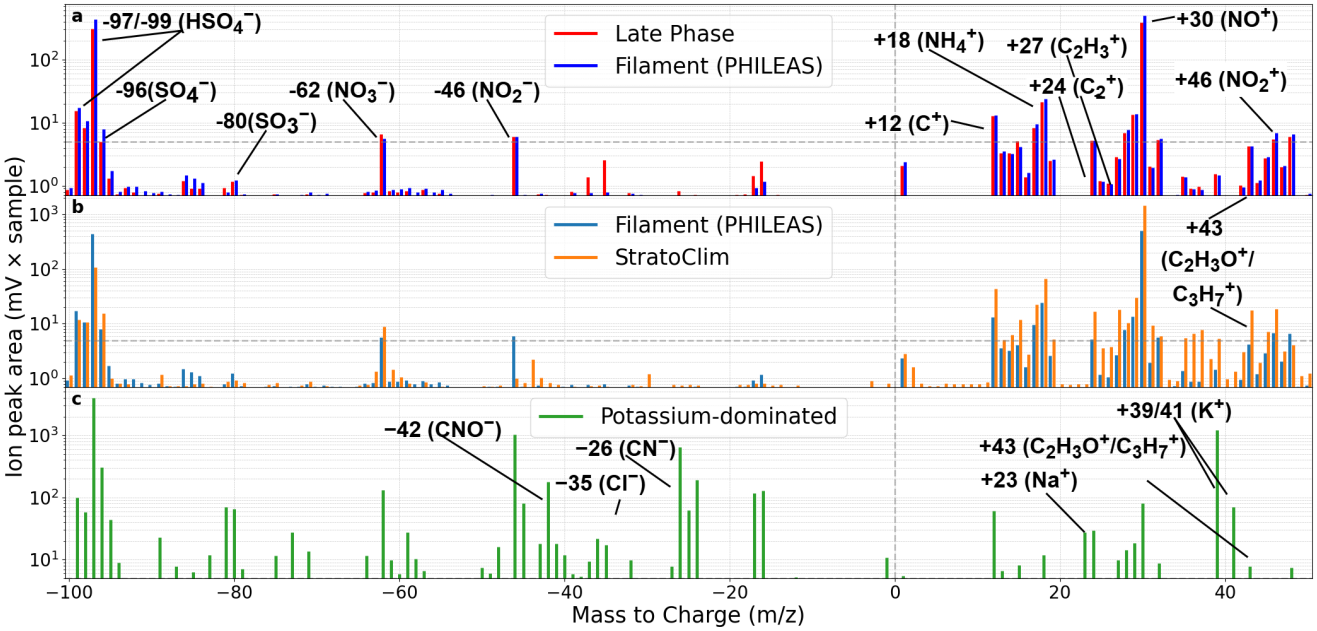

Figure S3. Bipolar mean spectra of the ERICA-LAMS NO^+-rich particle type: (a) Comparison between the Late Phase (red average over 9,182 spectra) and AMA filament (blue, average over 11,145 spectra) events in the ExLS. Key peaks include -97/-99 HSO_4^-, -96 SO_4^{2-}, -80 SO_3^-, -62 NO_3^-, -46 NO_2^-, +30 NO^+, and +18 NH_4^+. (b) Comparison between the AMA-Filaments and lower ATAL regimes measured during the StratoClim campaign (orange, average over 4,769 spectra), showing similar spectral patterns. (c) Mean spectrum of potassium-dominated particles (green, average over 5,151 spectra), characterized by dominant signals from +39/+41 K^+, along with +23 Na^+, -35 Cl^-, -26 CN^-, -62 NO_3^-, -97/-99 HSO_4^-, and -42 CNO^-.

S2.4 Size dependence of particle mass spectra characteristics

The laser ablation process using ERICA-LAMS can yield varying mass spectra characteristics for different particle sizes even within the same particle type. To minimize this size-dependent effect and to ensure comparable mass spectral characteristics across different measurement phases and campaigns (e.g., from the center of the AMA (during StratoClim) to the ExLS (during PHILEAS)), only particles with diameters between 200 and 500 nm were selected for this analysis. This selection was supported by an analysis of the relative frequency distributions of particle sizes for No+-rich particles measuring during StratoClim and PHILEAS, as described in the main text. The results indicate that the majority of NO^+-rich particles, approximately 94% for StratoClim and 86% for PHILEAS, are within this size range.

An additional motivation stems from findings during a laboratory-based campaign (the SIA-campaign (SPMS Intercomparison campaign at AIDA 2023)) conducted at the AIDA chamber (KIT) with the ERICA aerosol mass spectrometer in November and December of 2023. This experiment provided an opportunity to investigate the chemical properties of particles measured within the ATAL under controlled conditions simulating the ASM and AMA environment. It was observed that, for particle sizes above 500 nm, the ion signal intensity for single particles exhibited a dependence on particle size. The underlying

mechanisms remain uncertain and is subject of ongoing research. The results of this laboratory campaign will be published separately.

S2.5. Uncertainty Calculation Methods: ERICA-LAMS Dataset

In this section, we describe the methodologies employed to calculate the uncertainties of three output variables by ERICA-LAMS: (1) the particle fraction (Eq. 1), (2) the difference of particle fractions (Eq. 2-4), and (3) the ratio of ion signal intensities (Eq. 5).

(1) Particle fraction

For the vertical profiles showing particle fractions versus potential temperature, the uncertainty in the particle fraction was determined using the standard formula for binomial proportions. This method evaluates the fraction of particles of a specific type relative to the total particle count within each bin of potential temperature. The uncertainty was calculated for each bin, incorporating the statistical variability inherent in particle counting by using the formula taken from Appel et al. (2022a):

$$\sigma_{\mathrm{PF}}^{\mathrm{abs}} = \frac{\sqrt{N_{\mathrm{total}} \cdot f \cdot (1-f)}}{N_{\mathrm{total}}} \tag{1}$$

where:

- N_{total} is the total number of particles in a given bin,
- f is the particle fraction for the specific particle type, calculated as $f = \frac{N_{\mathrm{type}}}{N_{\mathrm{total}}}$,
- $\sigma_{\mathrm{PF}}^{\mathrm{abs}}$ is the uncertainty of the particle fraction.

(2) Difference of particle fraction

To evaluate the uncertainty of the change in the particle fraction between two different air mass periods ('Early Phase' and 'Late Phase'), we used the binomial statistics. Figure S4 shows the uncertainties of the change in particle fraction between the Late and Early Phases of PHILEAS. The calculation was conducted as follows: The fraction of specific particle types in each period was computed as:

$$f_{\mathrm{Early}} = \frac{N_{\mathrm{type,\ Early}}}{N_{\mathrm{total,\ Early}}}, \quad f_{\mathrm{Late}} = \frac{N_{\mathrm{type,\ Late}}}{N_{\mathrm{total,\ Late}}}, \quad f_{\mathrm{Diff}} = f_{\mathrm{Late}} - f_{\mathrm{Early}}, \tag{2}$$

where $N_{\mathrm{type,\ Early}}$ and $N_{\mathrm{type,\ Late}}$ represent the number of specific particle types observed during the Early Phase and Late Phase periods, respectively, and $N_{\mathrm{total,\ Early}}$ and $N_{\mathrm{total,\ Late}}$ are the total particle counts during those periods. f_{Diff} is the difference in the particle fraction between the Late and Early Phase.

The uncertainty was calculated as follows:

$$\sigma_{\mathrm{Early}} = \frac{\sqrt{N_{\mathrm{total,\ Early}} \cdot f_{\mathrm{Early}} \cdot (1-f_{\mathrm{Early}})}}{N_{\mathrm{total,\ Early}}}, \quad \sigma_{\mathrm{Late}} = \frac{\sqrt{N_{\mathrm{total,\ Late}} \cdot f_{\mathrm{Late}} \cdot (1-f_{\mathrm{Late}})}}{N_{\mathrm{total,\ Late}}}. \tag{3}$$

To account for the total uncertainty when comparing the two periods, the combined uncertainty for P_{Diff} was calculated as the root-sum-square of the individual uncertainties (σ_{Diff}):

$$\sigma_{\text{Diff}} = \sqrt{\sigma^2_{\text{Early}} + \sigma^2_{\text{Late}}}. \tag{4}$$

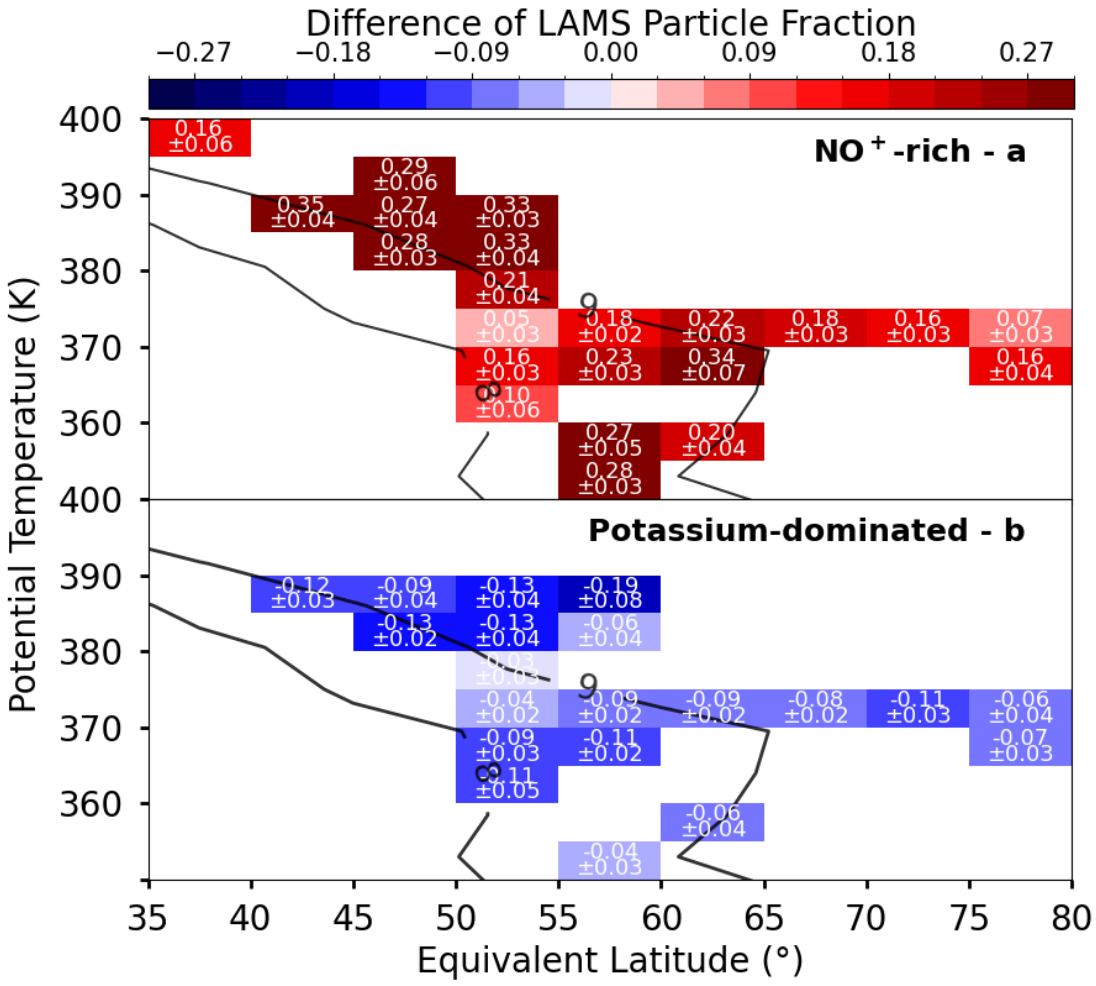

Figure S4. Mean distribution of ERICA-LAMS spectra based on the difference in particle fraction for NO^+-rich (a), potassium-dominated particles (b) between the Late and Early Phase, as a function of ERA5-derived equivalent latitude and potential temperature. The black solid lines indicate isolines of PV (derived from ERA5) in PVU. The overlaid white numbers in each bin indicate the particle fraction differences (top number) and its associated uncertainty (bottom number), calculated using uncertainty propagation (see Eqs. 2-4). The graph corresponds to Fig. 5 in the main text.

(3) Ratio of different ion signal intensities

The ion signal intensity ratio between two signals, such as m/z +18 and +30, is calculated using Eq. 5:

$$\mathrm{Ratio}_{x/y} = \frac{\overline{x}}{\overline{y}} \tag{5}$$

Here, $\overline{x}$ and $\overline{y}$ denote the mean ion signal intensities of the respective ion signal intensity ratios, averaged over the different phases (e.g., Early or Late Phase) as presented in this work. The uncertainty of the ion signal intensity ratios (σ_{ratio}) was calculated using the propagation of uncertainty, accounting for the independent variances of the numerator and denominator, as well as their covariance. The formula used for this calculation is:

$$\sigma_{\text{ratio}} = \frac{\sqrt{\left(\frac{\sigma_x}{\overline{y}}\right)^2 + \left(\frac{\sigma_y \cdot \overline{x}}{\overline{y}^2}\right)^2 - 2 \cdot \frac{\overline{x}}{\overline{y}^3} \cdot \frac{\sum(x_i - \bar{x})(y_i - \bar{y})}{n-1}}}{\sqrt{n}}, \tag{6}$$

where:

- $\overline{x}$ and $\overline{y}$ are the mean values of the ion signal intensities of the m/z ratio in the numerator and denominator, respectively,
- σ_x and σ_y are the standard deviations of the mean values $\overline{x}$ and $\overline{y}$, respectively,
- x_i and y_i represent the ion signal intensities of individual points contributing to the mean, and
- n is the total number of observations in the dataset.

The formula considers three components: (1) the contribution of the numerator variability ($\frac{\sigma_x}{y}$), (2) the contribution of the denominator's variability ($\frac{\sigma_y \cdot x}{y^2}$), and (3) the covariance term that accounts for the dependence between x_i and y_i with $\sum(x_i - \bar{x})(y_i - \bar{y})$. Finally, the normalization by $\sqrt{n}$ ensures the uncertainty scales with the sample size.

S3. ERICA-AMS: Data Evaluation

S3.1 Data Post-Processing and Data Analysis

A detailed description of the ERICA-AMS data structure is provided in the supplementary material of Appel et al. (2022a). In the TofWare 2.5.7 software, the settings were customized to meet the specific requirements of the ERICA-AMS data structure. To prevent the software from normalizing each spectrum to m/z 28, a method intended for Aerosol Chemical Speciation Monitor (ACSM) instruments, for which the software was originally developed, the command **'setigoroption poundde-fine=tw_ACSM_diffSticks_dontNorm28'** was executed. The software was then recompiled to apply this modification. Additionally, the **Background is blocked beam (adv)** option was enabled. Due to the custom-built shutter unit in our setup, the software was unable to automatically determine the shutter positions. This limitation was addressed by manually defining the positions: 2–12 for total measurements, 14–24 for background measurements, and buffer position 13 for switching. The mass calibration of the AMS species (such as nitrate, ammonium, organics, sulfate, and chloride) were achieved using the ionization

efficiency (IE) calibration, the relative ionization efficiency (RIE) factor (Tab. S4) and a reference flow rate of 1.45 cm^3/s (see S3.2). Furthermore, an m/z calibration was conducted to accurately identify ion signal peaks. A three-parameter fit, $p_1 \cdot m^{p_3} + p_2$, was applied using the following reference mass-to-charge ratios: CH^+ (m/z = 13.0078), O_2^+ (31.9898), SO_2^+ (63.9619), $^{182}W^+$ (181.948), $^{184}W^+$ (183.951), and $^{186}W^+$ (185.954). TofWare 2.5.7 was used to generate stick spectra based on these predefined parameters. Baseline correction for all spectra was performed by applying a linear interpolation method with an integration width of 13 and smoothing set to 2. The aerosol signal was calculated as the difference (diff spectrum) between the open-shutter and closed-shutter measurements. During each research flight, two filter measurements were taken and included into the data post-processing. In particular, filter measurements were used to adjust the fragmentation table in Tofware 2.5.7. Finally, all AMS data points during cloud interactions in flights were excluded using cloud flags provided by the BCPD instrument (Lucke et al., 2023).

S3.2 Ionization efficiency (IE) Calibration

A detailed description of the determination of the IE value for the ERICA-AMS dataset is provided in the supplementary material of Appel et al. (2022a). Values of the IE calibration that were conducted during ground-based operation in the hangar are listed in Tab. S4. For the post-processing of the ERICA-AMS dataset with the IE values, it is important to consider the wildfire event during F09 (28.08.2023). During this wildfire event, measurements were taken within a very intense wildfire plume over Canada at altitudes of around 3 km. While correcting the data, we observed that the organic concentration measured by the ERICA-AMS increased significantly after the wildfire event. We assume that our flexible O-ring (as a part of the CPI) was afterwards clogged probably with soot/organic particles for a while. We found indications for this hypothesis in the position settings of the O-ring control unit. As a result, we observed that the following IE value decreased from 2943.99 to 1486.42 $ions\ pg^{-1}$ after this event. Consequently, we processed F09 and all flights before F09 using the IE value of 2943.99 $ions\ pg^{-1}$. The dataset after F09 until F16 was processed using the IE value of 1486.42 $ions\ pg^{-1}$ for the dataset after the event.

For flights F16 and F17, we used the average of the IE calibration values obtained on 14.09.2023 and 18.09.2023. Finally, for all data after F17 we used the IE value of 2301.75 $ions\ pg^{-1}$.

Table S4. Overview of IE Calibrations for PHILEAS.

Date	SIS (mV*ns)	IE ($ions\ pg^{-1}$)	RIE (NH_4)	RIE (SO_4)	Valid for Flight
18.07.2023	0.713	4409.12	4.11304	0.838158	F02
25.08.2023	0.974	2943.99	4.24608	0.879123	F04 - F09
14.09.2023	0.974	1486.42	4.19520	0.594948	F09 - F15
14.09.2023	0.812	2040.79	4.72384	0.574809	–
18.09.2023	0.812	2456.42	4.41489	0.684701	–
Average of 14.09.–18.09.2023	0.812	2248.61	4.56937	0.629755	F16 - F17
18.09.2023	0.828	2301.75	4.36447	0.720949	F18 - F20

S3.3 Detection Limits

The determination of the detection limits (DLs) for nitrate, sulfate, ammonium and organic matter is analogous to the evaluation described in Appel et al. (2022a). The DLs for PHILEAS were calculated point-by-point. The average DLs for the Late and Early Phases are presented in Tab. 2 in the main text. It should be noted that the average DLs became slightly higher over the course of the campaign (from the Early to the Late Phase). We assume that the same factor that influenced the IE also influenced the detection limit at the same time.

Furthermore, we determined the DLs for each bin in order to asses whether ambient concentrations are above the DLs with Eq. 7 (see Fig. S5).

$$\mathrm{DL}_{\text{bin}} = \mathrm{mean}\left(\mathrm{DL}_i\right) \tag{7}$$

To account for statistical uncertainty in bins with fewer data points, we further adjusted the DLs using the standard error of the mean (SEM) principle:

$$\mathrm{DL}_{\text{bin, adjusted}} = \frac{\mathrm{DL}_{\text{bin}}}{\sqrt{n}} \tag{8}$$

where n is the number of data points in the respective bin. Bins containing fewer than 10 data points were excluded from the analysis to ensure statistical reliability. Additionally, we determined vertically resolved profiles of aerosol concentration as a function of potential temperature, including error bars that reflect the SEM, calculated from the bin-wise standard deviation:

$$\mathrm{SEM}_\theta = \frac{s}{\sqrt{n}} \tag{9}$$

where s denotes the sample standard deviation of the concentration values in a given θ-bin. These profiles were plotted separately for Early and Late Phases, providing further context for phase related aerosol differences across the ExLS background.

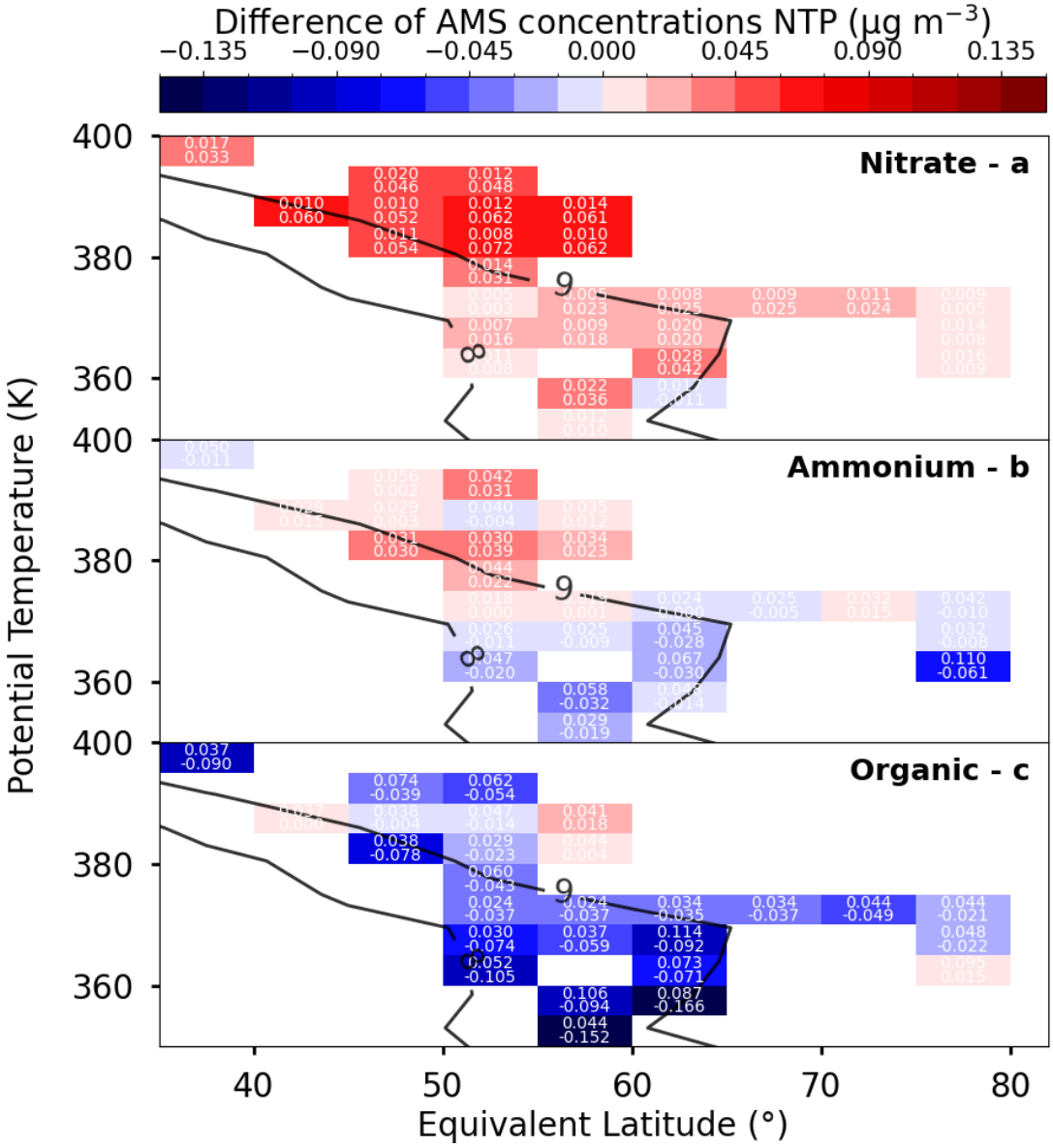

Figure S5. Mean distribution of ERICA-AMS nitrate (a), ammonium (b), and organic matter (c) mass concentrations, shown as the difference between the Late and Early Phases, as a function of ERA5-derived equivalent latitude and potential temperature. Black contours indicate isolines of potential vorticity (ERA5-derived) in PVU. The white numbers inside each bin represent the concentration difference (bottom number) and the detection limit (top number) in μg m^{-3} at NTP conditions. Bins with fewer than 10 data points were excluded. The graph corresponds to Fig. 4a-c in the main publication.

S4. Identification of Stratospheric Background Air Masses

Measurements of trace gases like N_2O and CO are essential for characterizing stratospheric background air masses and air masses influenced by pollution events, such as from the ASM region (e.g., Müller, 2015; Müller et al., 2016). In this case, the UMAQS dataset was used to categorize all ERICA-AMS and ERICA-LAMS measurements according to stratospheric background criteria. First, all flight data were combined and measurements with N_2O mixing ratios below 336 ppbv were classified as stratospheric air masses (Riese et al., 2025). Second, within this subset, CO measurements were used to further differentiate between stratospheric background and recently polluted stratospheric air masses. To accomplish this, a relative frequency distribution of all CO data points in the stratosphere ($N_2O < 336$ ppbv) were constructed using 1 ppbv bin widths. The resulting distribution is shown in Fig. S6a. Based on the observed bimodality, a threshold of 40 ppbv CO was defined to separate background stratospheric air from polluted events such as from ASM air masses. To evaluate the reliability of this threshold-based approach, ERA5-derived PV values were used as an independent diagnostic for stratospheric air masses. Figure S6b presents the relative frequency distribution of PV values for all data classified with $N_2O < 336$ ppbv and CO < 40 ppbv. The vast majority of these classified air masses exhibit high PV values (greater than 8 PVU), which is indicative of stratospheric origin. This comparison confirms that the chosen in-situ thresholds (N_2O and CO) reliably identify stratospheric background air. Consequently, for this study, $N_2O < 336$ ppbv and CO < 40 ppbv were used as the primary criteria for filtering both in-situ measurement data and CLaMS modeling results.

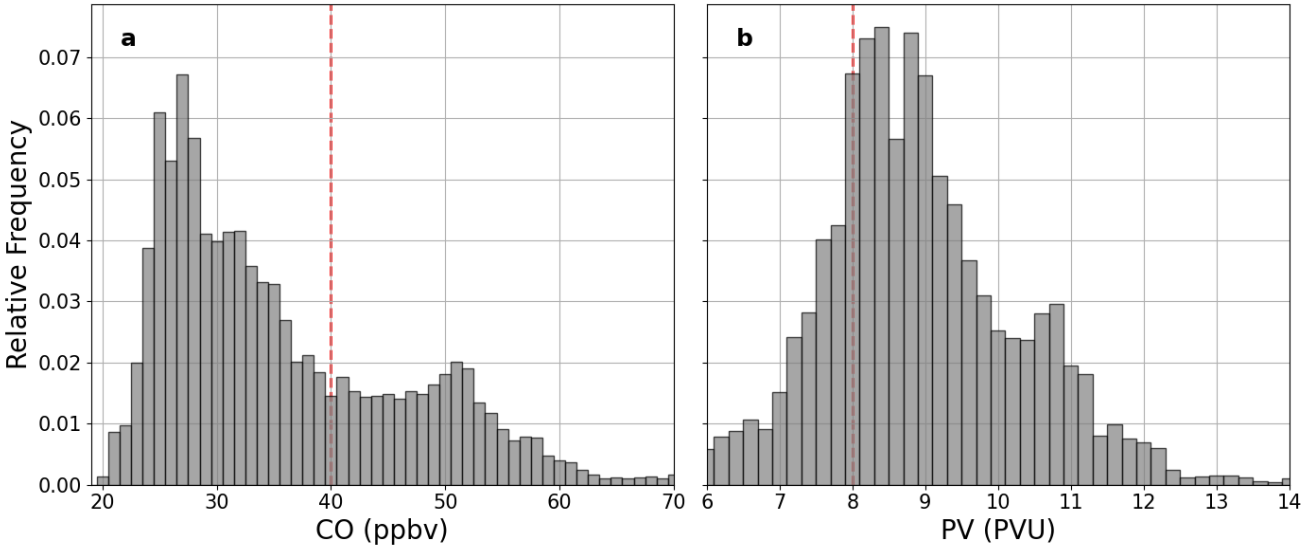

Figure S6. Relative frequency distributions of (a) CO for all data with $N_2O < 336$ ppbv and (b) ERA5-derived PV for data with both $N_2O < 336$ ppbv and CO < 40 ppbv. Red dashed lines indicate the applied thresholds for stratospheric background air (CO < 40 ppbv, PV > 8 PVU). The bimodal distribution in (a) illustrates the separation between stratospheric background air and recently polluted stratospheric air masses. The distribution in (b) demonstrates that data selected using the N_2O and CO thresholds also show high PV values (> 7 PVU), thus independently confirming that these criteria reliably identify stratospheric air masses.

S5. CLaMS Backwards Trajectories for Early and Late Phase

A complete picture of transport characteristics outside the core ASM influenced layer was provided by examining backward trajectory statistics for air masses below 320 K and above 380 K potential temperature.

At potential temperatures below 320 K, the trajectory distributions show a significant seasonal shift between the initial Early and Late Phases of the campaign. The corresponding trajectory distributions are shown in Fig. S7. During the Early Phase, the densities of the trajectories are dominated by maritime source regions, which is consistent with convective uplift over the Indian Ocean and the western Pacific. In contrast, the Late Phase shows a stronger contribution from the continental South Asian boundary layer, with enhanced trajectory densities over the Indian subcontinent and along the southern slopes of the Tibetan Plateau. This shift reflects the increasing importance of continental convection as the monsoon season progresses.

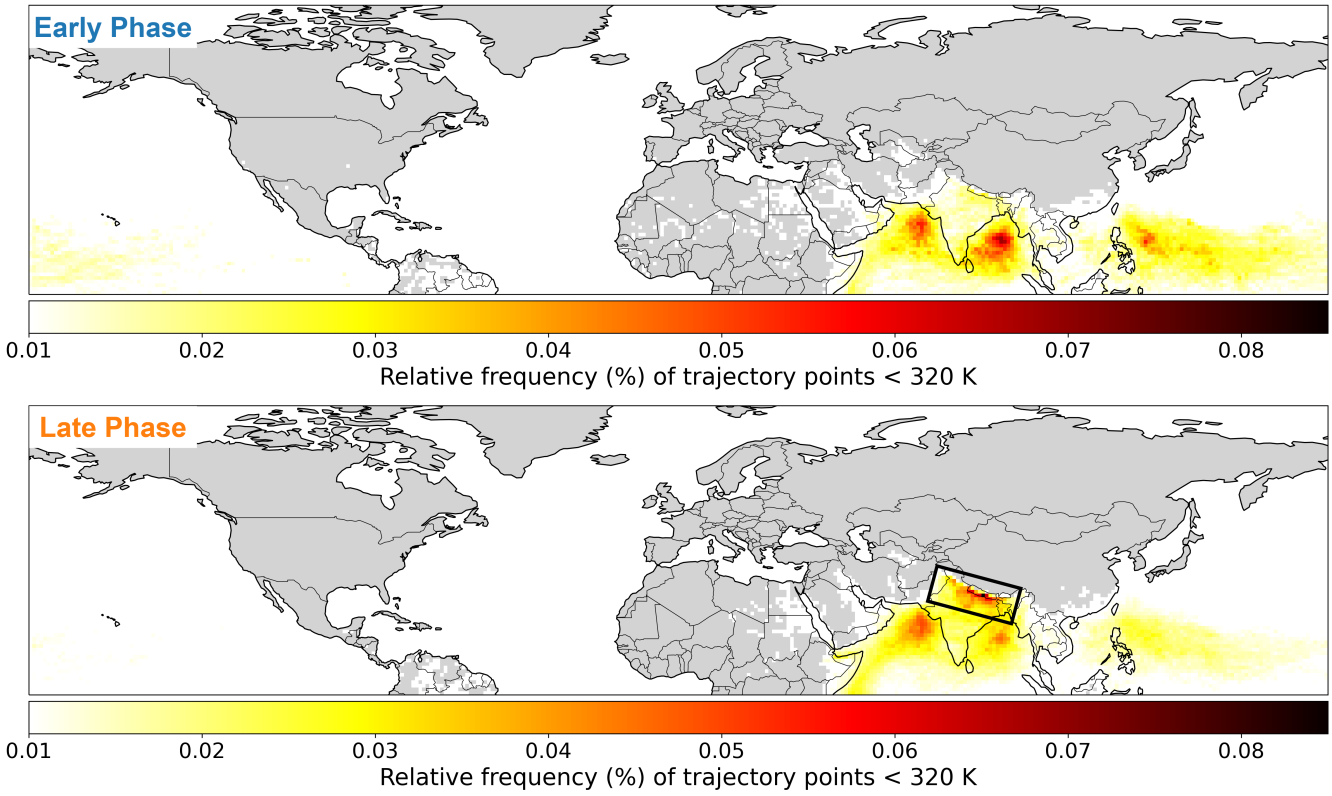

Figure S7. The figure shows the relative frequency of CLaMS backward trajectory points below 320 K potential temperature during the Early and Late Phases of the PHILEAS campaign. During the Early Phase, the densities of the trajectories are dominated by maritime source regions, which is consistent with convective uplift over the Indian Ocean and the western Pacific. During the Late Phase, there is an increased contribution from the continental South Asian boundary layer, resulting in enhanced trajectory occurrence over the Indian subcontinent and along the southern slopes of the Tibetan Plateau. This seasonal shift (illustrated in black frame in Late Phase) reflects the growing importance of continental convection as the ASM progresses.

At potential temperatures above 380 K, trajectory analysis reveals a distinct transport regime in both phases. The trajectory points form an extended band that extends across the equator and is associated with the extratropical westerly circulation. This band links North America, the North Atlantic, Europe, and Eurasia. This pathway is present throughout the campaign but appears broader and more zonally continuous during the Late Phase. This suggests particularly efficient, large-scale transport in this layer. This transport pattern primarily reflects lower stratospheric circulation rather than direct uplift by the ASM, the corresponding results are shown in Fig. S8.

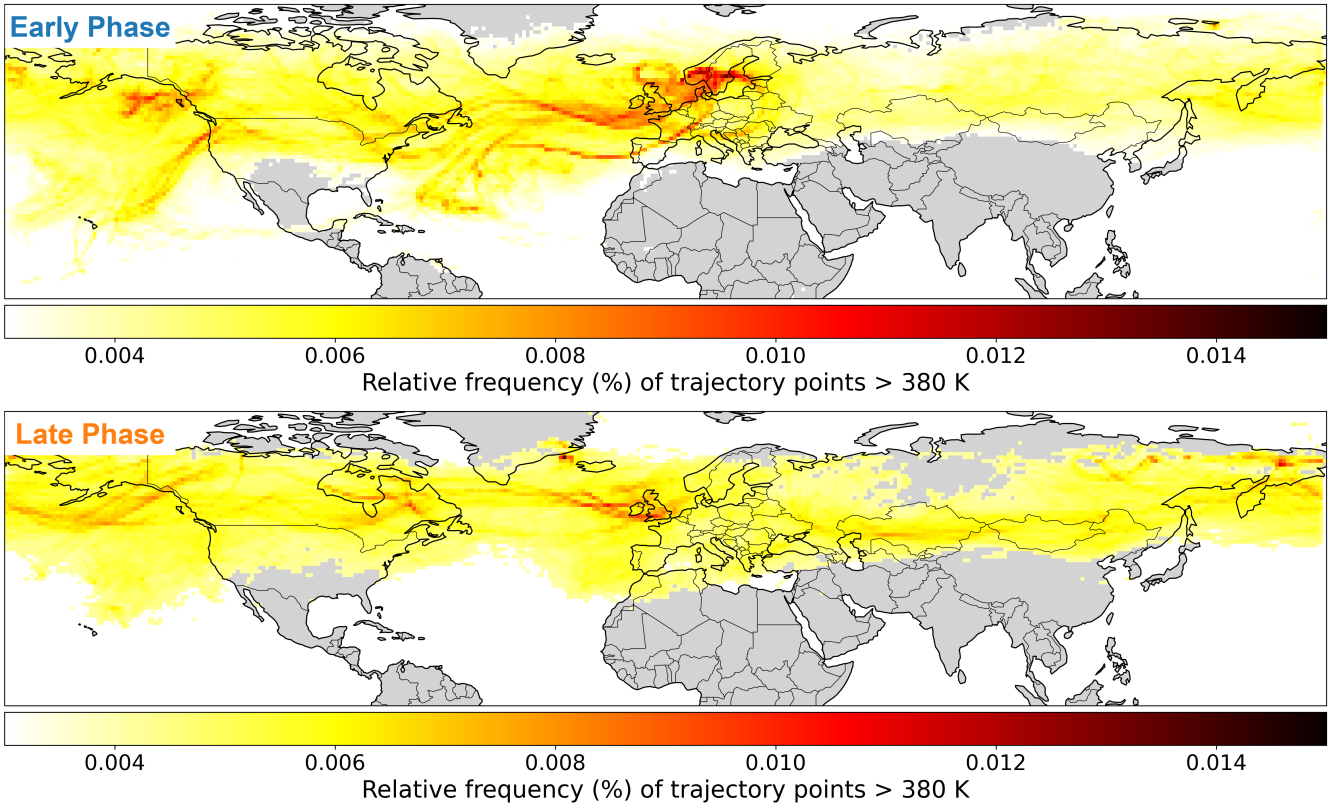

Figure S8. This graph shows the relative frequency of CLaMS backward trajectory points above 380 K potential temperature for the Early and Late Phases of the PHILEAS campaign. In both phases, the trajectory points form an extended band across the globe, which is associated with extratropical westerly circulation and links North America, the North Atlantic, Europe, and Eurasia. During the Late Phase, this transport pathway appears broader and more zonally continuous, indicating particularly efficient large-scale transport in this layer. The observed patterns primarily reflect lower stratospheric circulation rather than direct uplift by the ASM.

Despite the dominance of large-scale transport at these higher potential temperature regimes, the Late Phase exhibits an increased contribution of air masses originating from the South Asian boundary layer and, to a lesser extent, the western Pacific.

References

Andreae, M. O., Afchine, A., Albrecht, R., Holanda, B. A., Artaxo, P., Barbosa, H. M. J., Borrmann, S., Cecchini, M. A., Costa, A., Dollner, M., Fütterer, D., Järvinen, E., Jurkat, T., Klimach, T., Konemann, T., Knote, C., Krämer, M., Krisna, T., Machado, L. A. T., Mertes, S., Minikin, A., Pöhlker, C., Pöhlker, M. L., Pöschl, U., Rosenfeld, D., Sauer, D., Schlager, H., Schnaiter, M., Schneider, J., Schulz, C., Spanu, A., Sperling, V. B., Voigt, C., Walser, A., Wang, J., Weinzierl, B., Wendisch, M., and Ziereis, H.: Aerosol characteristics and particle production in the upper troposphere over the Amazon Basin, Atmospheric Chemistry and Physics, 18, 921–961, https://doi.org/10.5194/acp-18-921-2018, 2018.

Appel, O., Borrmann, S., et al.: Chemical analysis of the Asian tropopause aerosol layer (ATAL) with emphasis on secondary aerosol particles using aircraft-based in situ aerosol mass spectrometry, https://doi.org/10.5194/acp-22-13607-2022, supplement of Atmos. Chem. Phys., 22, 13607–13630, 2022a.

Appel, O., Köllner, F., Dragoneas, A., Hünig, A., Molleker, S., Schlager, H., Mahnke, C., Weigel, R., Port, M., Schulz, C., Drewnick, F., Vogel, B., Stroh, F., and Borrmann, S.: Chemical analysis of the Asian tropopause aerosol layer (ATAL) with emphasis on secondary aerosol particles using aircraft-based in situ aerosol mass spectrometry, Atmospheric Chemistry and Physics, 22, 13 607–13 630, https://doi.org/10.5194/acp-22-13607-2022, 2022b.

Klimach, T.: Chemische Zusammensetzung der Aerosole: Design und Datenauswertung eines Einzelpartikel-Laserablationsmassenspektrometers, Ph.D. thesis, Johannes Gutenberg University Mainz, https://doi.org/10.25358/openscience-4386, 2012.

Kulkarni, P., Baron, P. A., and Willeke, K., eds.: Aerosol Measurement: Principles, Techniques, and Applications, John Wiley & Sons, Hoboken, New Jersey, 3rd edn., ISBN 978-0-470-38741-2, 2011.

Köllner, F., Schneider, J., Willis, M. D., Klimach, T., Helleis, F., Bozem, H., Kunkel, D., Hoor, P., Burkart, J., Leaitch, W. R., Aliabadi, A. A., Abbatt, J. P. D., Herber, A. B., and Borrmann, S.: Particulate trimethylamine in the summertime Canadian high Arctic lower troposphere, Atmospheric Chemistry and Physics, 17, 13 747–13 766, https://doi.org/10.5194/acp-17-13747-2017, 2017.

Lucke, J. R., Jurkat, T., Baumgardner, D., Kalinka, F., Moser, M., De La Torre Castro, E., and Voigt, C.: Characterization of Atmospheric Icing Conditions during the HALO-(AC) Campaign with the Nevzorov Probe and the Backscatter Cloud Probe with Polarization Detection, SAE Technical Paper, https://doi.org/10.4271/2023-01-1485, 2023.

Minikin, A., Sauer, D., Ibrahim, A., Franke, H., Röschenthaler, T., Fütterer, D., and Petzold, A.: The HALO Submicrometer Aerosol Inlet (HASI): Design Concept and First Characterization, poster presented at the HALO Symposium 2017, Oberpfaffenhofen, Germany, 2017.

Müller, S.: Untersuchung von Mischungs- und Transportprozessen in der oberen Troposphäre - unteren Stratosphäre basierend auf in-situ Spurengasmessungen, Ph.D. thesis, Mainz, https://doi.org/http://doi.org/10.25358/openscience-1807, 2015.

Müller, S., Hoor, P., Bozem, H., Gute, E., Vogel, B., Zahn, A., Bönisch, H., Keber, T., Krämer, M., Rolf, C., Riese, M., Schlager, H., and Engel, A.: Impact of the Asian monsoon on the extratropical lower stratosphere: trace gas observations during TACTS over Europe 2012, Atmospheric Chemistry and Physics, 16, 10 573–10 589, https://doi.org/10.5194/acp-16-10573-2016, 2016.

Riese, M., Hoor, P., Rolf, C., Kunkel, D., Vogel, B., Köllner, F., Pöhlker, M., Ploeger, F., Ungermann, J., Woiwode, W., Johansson, S., Bauer, R., Barmpounis, K., Borrmann, S., Brauner, P., Clemens, J., Dragoneas, A., Ekinci, F., Emig, N., Engel, A., Eppers, O., Fadnavis, S., Friedl-Vallon, F., Geldenhuys, M., Günther, G., Grooß, J., Hegglin, M., Höpfner, M., Jesswein, M., Joppe, P., Kaumanns, J., Kachula, O., Keber, T., Kretschmer, E., Lachnitt, H., Lauther, V., Lloyd, P., Molleker, S., Müller, R., Neubert, T., Ort, L., Pöschl, U., Pöhlker, C., Rapp, M., Retzlaff, M., Rhode, S., Schneider, J., Schuck, T., Sinnhuber, B., Spelten, N., Strobel, J., Tomsche, L., Turhal, K., van Luijt, R.,

Versick, S., Voigt, C., Volk, M., von Hobe, M., Weyland, F., Zahn, A., Ziereis, H., and Zlotos, L.: Long-range transport of polluted Asian summer monsoon air to high latitudes during the PHILEAS campaign in the boreal summer 2023, Bulletin of the American Meteorological Society, https://doi.org/10.1175/BAMS-D-24-0232.1, early Online Release, 2025.